23 Jan 2024

Quaternary Rare-Earth Oxyselenides RE4Ga2Se7O2 (RE = Pr, Nd) With Trigonal Bipyramidal GaSe5 Units: Evaluation Of Optical, Thermoelectric, And Electrocatalytic Properties

Vidyanshu Mishra

Ibrahim Munkaila Abdullahi

Dundappa Mumbaraddi

Mohammed Jomaa

et. al. For a complete list of authors, see https://scholarsmine.mst.edu/chem_facwork/3680

Recommended Citation

V. Mishra et al., "Quaternary Rare-Earth Oxyselenides RE4Ga2Se7O2 (RE = Pr, Nd) With Trigonal Bipyramidal GaSe5 Units: Evaluation Of Optical, Thermoelectric, And Electrocatalytic Properties," *Chemistry of Materials*, vol. 36, no. 2, pp. 937 - 948, American Chemical Society, Jan 2024.
The definitive version is available at https://doi.org/10.1021/acs.chemmater.3c02842

CHEMISTRY OF MATERIALS

pubs.acs.org/cm

Article

Quaternary Rare-Earth Oxyselenides $RE_4Ga_2Se_7O_2$ (RE = Pr, Nd) with Trigonal Bipyramidal $GaSe_5$ Units: Evaluation of Optical, Thermoelectric, and Electrocatalytic Properties

Published as part of Chemistry of Materials virtual special issue "C. N. R. Rao at 90".

Vidyanshu Mishra, Ibrahim Munkaila Abdullahi, Dundappa Mumbaraddi, Mohammed Jomaa, Louis Guérin, Manashi Nath,* and Arthur Mar*

Cite This: *Chem. Mater.* 2024, 36, 937−948

Read Online

ACCESS | Metrics & More | Article Recommendations | Supporting Information

ABSTRACT: Phase-pure samples and single crystals of the rare-earth oxyselenides $RE_4Ga_2Se_7O_2$ (RE = Pr, Nd) were prepared by reactions at 950 °C. They adopt a new structure type (orthorhombic, space group *Pnma*, a = 11.721(2)−11.683(2) Å, b = 3.9882(7)−3.9667(7) Å, c = 29.644(5)−29.581(5) Å, Z = 4) consisting of $RESe_6$ trigonal prisms, $GaSe_4$ tetrahedra, and $GaSe_5$ trigonal bipyramids linked to form corrugated layers between which strips of edge-sharing RE_4O tetrahedra are inserted. The bonding character is mostly ionic within RE−O and RE−Se blocks but mostly covalent with Ga−Se blocks, as supported by electronic structure calculations. Both compounds show a nearly direct optical band gap of 1.7 eV. Their Seebeck coefficients and electrical conductivities are predicted to be similar to other oxychalcogenides, with the thermoelectric power factors being improved by n-doping. They exhibit high electrocatalytic performance for the oxygen evolution reaction, with the Pr member demonstrating superior activity, as characterized by a low overpotential of 257 mV (at a current density of 10 mA cm^{-2}), a high mass activity of 70.1 A g^{-1}, and a turnover frequency of 0.0234 s^{-1} in 1 M KOH electrolyte.

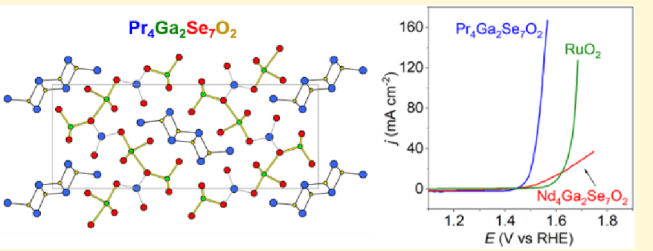

1. INTRODUCTION

Introducing more than one type of anion in a solid state compound offers greater flexibility to control its chemical and physical properties, by taking advantage of the different electronegativities, sizes, polarizabilities, and oxidation states of diverse combinations of nonmetals.[1−3] Among mixed-anion compounds, oxychalcogenides are the best known but even these remain underinvestigated: <1000 oxychalcogenides have been structurally characterized compared to >50 000 oxides.[4] Based on the hypothesis that local coordination environments around metal atoms can become more asymmetric and that band gaps can be narrowed relative to oxides, oxychalcogenides have received considerable attention as candidates for optical and thermoelectric materials, among many applications.[5−13] Another hypothesis is that multiple anions lead to complex changes in the electronic structure around active sites in oxychalcogenides used as catalysts for water splitting, so that they exhibit intermediate characteristics that balance the requirements of structural stability and electrochemical performance.[14−17]

Incorporating rare-earth metals into these oxychalcogenides greatly expands possibilities. Ternary rare-earth oxysulfides RE_2SO_2 were one of the earliest examples of mixed-anion compounds, being used as phosphors in cathode ray tubes.[18] Quaternary rare-earth oxychalcogenides RE−M−Ch−O (M = d- or p-block metals or metalloids) have been identified to be potentially useful as thermoelectrics ($LaBiCh_2O$),[19] transparent semiconductors (LaCuSO),[20] superconductors ($LaBiS_2O_{1-x}$),[21] ionic conductors (LaAgSO),[22] and photocatalysts ($Sm_2Ti_2S_2O_5$).[23] To the best of our knowledge, none of these rare-earth oxychalcogenides have been investigated for their electrocatalytic activity. The high cost and scarcity of precious metals and their oxides, currently used as electrocatalysts for water splitting, provide impetus to evaluate other candidates.[24] Rare-earth-containing compounds (including alloys, oxides, and hybrid materials) have been proposed as attractive candidates for electrocatalysis.[25]

Within the quaternary systems RE−M−Ch−O (M = Ga, In; Ch = S, Se), previously known compounds include $REMCh_2O$ (M = Ga, In; Ch = S, Se),[26−33] $RE_4Ga_2Ch_5O_4$ (Ch = S,

Received: November 6, 2023
Revised: December 21, 2023
Accepted: December 26, 2023
Published: January 2, 2024

Se),[29,34,35] $RE_4Ga_{1.33}S_4O_4$,[29] $La_{3.33}Ga_6S_{12}O_2$,[36] RE_3GaCh_5O (*Ch* = S, Se),[37,38] $La_5In_3S_9O_3$,[30] $La_{10}In_6S_{17}O_6$,[39] $La_4Ga_2Se_6O_3$,[40] and $La_4Ga_2S_8O_3$.[41] Some of these compounds ($REMCh_2O$, La_3GaS_5O, and $La_5In_3S_9O_3$) have been evaluated for photocatalytic activity in water splitting reactions.[31−33,41−43] The compound Sm_3GaSe_5O was discovered inadvertently as a result of targeting the hypothetical solid solutions $RE_3MCh_{6-x}O_x$, based on the existence of the ternary phases RE_3MCh_6.[38] It is becoming clear that the structures of rare-earth oxychalcogenides cannot be extrapolated in a simple way from chalcogenides and that more complex structure-building principles are at play in these mixed-anion systems.[44,45] In particular, there is a preference for the *RE* and O atoms to be bonded together in recurring structural motifs involving RE_4O tetrahedra. Furthermore, in contrast to the observation that sulfides and selenides are often isostructural, the assumption does not necessarily extend to oxysulfides and oxyselenides; for example, notwithstanding their identical compositions, $LaGaS_2O$ and $LaGaSe_2O$ have different structures.[27,28]

Given this background, it is worthwhile to prepare and characterize further oxyselenides, which remain few compared to the corresponding oxysulfides. Here, we report the synthesis of oxyselenides $RE_4Ga_2Se_7O_2$ (*RE* = Pr, Nd) and their structure determination. To evaluate their potential as optical and thermoelectric materials, their optical band gaps were measured and their transport properties were predicted from first-principles calculations. These compounds were also investigated for electrocatalytic activity in the oxygen evolution reaction (OER) for water splitting.

2. EXPERIMENTAL SECTION

2.1. Synthesis. Starting materials were freshly filed *RE* pieces (*RE* = Pr, Nd; 99.9%, Hefa), nominally Pr_6O_{11} or Nd_2O_3 powders (99.99%, Sigma-Aldrich), Ga chunks (99.9%, Alfa-Aesar), and Se powder (99.99%, Sigma-Aldrich). Ga_2Se_3 was prepared by heating a stoichiometric mixture of Ga and Se at 950 °C in evacuated and sealed fused-silica tubes.

The oxyselenides $RE_4Ga_2Se_7O_2$ (*RE* = Pr, Nd) were initially identified in the course of targeting hypothetical solid solutions $RE_3MCh_{6-x}O_x$ (*M* = Ga, In; *Ch* = S, Se). Rational syntheses were subsequently developed. In typical reactions, the starting materials were combined in appropriate molar ratios to give a total mass of 300 mg, with a 5% weight excess of Se added to compensate for volatilization losses. The mixtures were pressed into pellets and placed in fused-silica tubes (12 mm diameter and 15 cm length), which were evacuated, sealed, and heated according to the temperature profiles detailed below. The small total mass of reactants relative to the large size of the tubes minimizes the risks of explosions in sealed-tube reactions. For $Nd_4Ga_2Se_7O_2$, the reaction of a mixture of Nd, Nd_2O_3, Ga_2Se_3, and Se in the molar ratio of 8:2:3:12, which matches with the desired composition, resulted in phase-pure samples. For $Pr_4Ga_2Se_7O_2$, the matter was slightly more complicated. After some effort, it was ascertained from powder X-ray diffraction (XRD) analysis that the as-purchased starting material labeled as Pr_6O_{11} consisted of PrO_2. Binary oxides of praseodymium, which adopt a range of variable compositions $PrO_{2-\delta}$, are prone to undergo phase transformations depending on thermal treatments.[46] With the assumption that the commercial starting material is better represented as PrO_2, the reaction of a mixture of Pr, PrO_2, Ga_2Se_3, and Se in the molar ratio of 3:1:1:4 resulted in phase-pure samples of $Pr_4Ga_2Se_7O_2$.

For the growth of single crystals, the tubes were heated to 950 °C in 24 h, held there for 72 h, cooled to 400 °C in 96 h, and then cooled to room temperature by shutting off the furnace. Thin, needle-shaped, dark brown single crystals of $Pr_4Ga_2O_2Se_7$ and $Nd_4Ga_2O_2Se_7$ were found in the products (Figure S1) and examined on a Zeiss Sigma 300 VP field emission scanning electron microscope operated with an accelerating voltage of 15 kV and equipped with a Bruker Quantax 600 system with dual X-Flash 6/60 detectors, which allows light elements to be analyzed. Energy-dispersive X-ray (EDX) analysis indicated an average composition (in mol %) of 24−25% *RE*, 10−11% Ga, 46−47% Se, and 16−19% O, in good agreement with expectations (27% *RE*, 13% Ga, 47% Se, and 13% O).

For the preparation of phase-pure samples, the tubes were heated to 950 °C in 18 h, held there for 48 h, and cooled to room temperature in 18 h. Powder XRD patterns were collected on a Bruker D8 Advance X-ray diffractometer equipped with a Cu $K\alpha_1$ radiation source operated at 40 kV and 40 mA. XRD patterns recollected after a few months were unchanged, confirming that the samples are air-stable (Figure 1). Some of the peaks in the experimental patterns tend to be more intense than expected (especially the 008 peak near 24° and the 0,0,10 peak near 30°), consistent with the tendency for preferred orientation, which would be expected for the needle-shaped crystallites. Attempts were made to synthesize other *RE* analogues of these compounds under the same conditions as described above, but were unsuccessful.

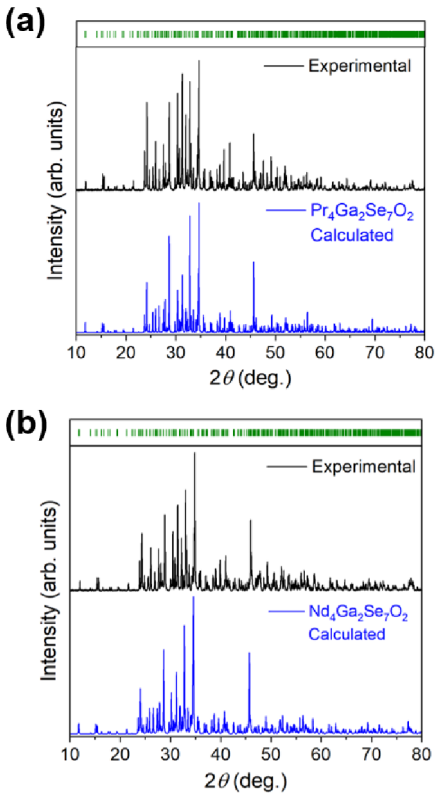

Figure 1. Powder XRD patterns for (a) $Pr_4Ga_2Se_7O_2$ and (b) $Nd_4Ga_2Se_7O_2$. The green bars indicate the positions of the Bragg peaks.

2.2. Structure Determination. Intensity data were collected on single crystals of $Pr_4Ga_2Se_7O_2$ and $Nd_4Ga_2Se_7O_2$ at room temperature on a Bruker PLATFORM diffractometer equipped with a SMART APEX II CCD area detector and a graphite-monochromated Mo Kα radiation source, using ω scans at 4−8 different ϕ angles with a frame width of 0.3° and an exposure time 60 s per frame. Multiscan absorption corrections were applied. Structure solution and refinement were carried out with use of the SHELXTL (version 2018/3) program package.[47]

On the basis of Laue symmetry, intensity statistics, and systematic absences, the orthorhombic space group *Pnma* was chosen. The locations of four *RE*, two Ga, and seven Se atoms were located by direct methods. Two additional peaks were found in difference electron density maps and assigned as the O atoms. Refinements were

https://doi.org/10.1021/acs.chemmater.3c02842
Chem. Mater. 2024, 36, 937−948

straightforward, with no indication for disorder, based on the reasonable displacement parameters found for all atoms and the observed bond distances in agreement with expectations. When the occupancies of each site were refined, they converged to unity. Atomic positions were standardized with the program STRUCTURE TIDY.[48] Table 1 lists crystal data, Table 2 lists atomic and displacement parameters, and Table 3 lists interatomic distances. Further data have been deposited in the Supporting Information.

Table 1. Crystallographic Data for $RE_4Ga_2Se_7O_2$ (*RE* = Pr, Nd)

formula	$Pr_4Ga_2Se_7O_2$	$Nd_4Ga_2Se_7O_2$
formula mass (amu)	1287.80	1301.12
space group	*Pnma* (no. 62)	*Pnma* (no. 62)
a (Å)	11.721(2)	11.683(2)
b (Å)	3.9882(7)	3.9667(7)
c (Å)	29.644(5)	29.581(5)
V (Å^3)	1385.8(4)	1370.8(4)
Z	4	4
T (K)	296(2)	296(2)
ρ_{calcd} (g cm^{-3})	6.173	6.304
crystal dimensions (mm)	0.08 × 0.02 × 0.01	0.17 × 0.03 × 0.02
μ(Mo $K\alpha$) (mm^{-1})	35.98	37.30
transmission factors	0.426–0.673	0.572–0.746
2θ limits	2.75–59.29°	3.75–59.64°
data collected	$-16 \le h \le 16$, $-5 \le k \le 5$, $-41 \le l \le 41$	$-16 \le h \le 16$, $-5 \le k \le 5$, $-41 \le l \le 41$
no. of data collected	19586	37878
no. of unique data, including $F_o^2 < 0$	2228 (R_{int} = 0.127)	2232 (R_{int} = 0.148)
no. of unique data, with $F_o^2 > 2\sigma(F_o^2)$	1499	1640
no. of variables	91	91
$R(F)$ for $F_o^2 > 2\sigma(F_o^2)$[a]	0.051	0.041
$R_w(F_o^2)$[b]	0.139	0.096
goodness of fit	1.03	1.03
$(\Delta\rho)_{max}$, $(\Delta\rho)_{min}$ (e Å^{-3})	2.90, − 3.78	2.51, − 3.32

[a]$R(F) = \sum||F_o| - |F_c||/\sum|F_o|$. [b]$R_w(F_o^2) = [\sum[w(F_o^2 - F_c^2)^2]/\sum wF_o^4]^{1/2}$; $w^{-1} = [\sigma^2(F_o^2) + (Ap)^2 + Bp]$, where $p = [\max(F_o^2,0) + 2F_c^2]/3$.

2.3. Calculations. Electronic structure calculations were performed on $Pr_4Ga_2Se_7O_2$ and $Nd_4Ga_2Se_7O_2$ using the projected augmented wave (PAW) method as implemented in the Vienna ab initio simulation package (VASP).[49] Exchange and correlation were treated in this density functional theory (DFT) method by the generalized gradient approximation, as parametrized by Perdew, Burke, and Ernzerhof (PBE).[50] Standard PAW potentials Pr_3, Nd_3, Se, Ga_d, and O were used, with the plane-wave basis cutoff energy set to 550 eV. To evaluate the density of states (DOS), a 12 × 35 × 5 gamma-centered k-mesh was chosen to sample the first Brillouin zone. The convergence criteria were set to 10^{-8} eV for electronic relaxation and $|-2 \times 10^{-2}|$ for ionic relaxation. Electron localization function (ELF) plots were prepared using VESTA, and a Bader analysis was performed to evaluate charges on atoms.[51−53] Chemical bonding was examined by assessing crystal orbital Hamilton populations (COHP) and crystal orbital bond indices (COBI) using the program Local Orbital Basis Suite Toward Electronic Structure Reconstruction (LOBSTER).[54−56] Transport properties were calculated using the BoltzTraP2 code, with the constant relaxation time approximation applied to interpolate the band structure obtained by DFT calculations.[57]

2.4. Diffuse Reflectance Spectroscopy. Optical diffuse reflectance spectra for $Pr_4Ga_2O_2Se_7$ and $Nd_4Ga_2O_2Se_7$ were measured from 200 nm (6.2 eV) to 1400 nm (0.8 eV) on a Cary 5000 UV−vis-NIR spectrophotometer equipped with a diffuse reflectance accessory. An optical polytetrafluorethylene disc with >98% reflectivity in the range of 250−2200 nm was used as a reflectance standard. The reflectance spectra were converted to absorption spectra using the Kubelka−Munk function, $F(R) = \alpha/S = (1 - R)^2/2R$, where α is the Kubelka−Munk absorption coefficient, S is the scattering coefficient, and R is the reflectance.[58]

Table 2. Atomic Coordinates[a] and Equivalent Isotropic Displacement Parameters for $RE_4Ga_2Se_7O_2$ (*RE* = Pr, Nd)

atom	x	y	z	U_{eq} (Å^2)[b]
$Pr_4Ga_2Se_7O_2$				
Pr1	0.23596(9)	1/4	0.05905(3)	0.0146(2)
Pr2	0.36342(9)	1/4	0.66841(4)	0.0149(2)
Pr3	0.49675(11)	1/4	0.81643(4)	0.0228(3)
Pr4	0.53559(9)	1/4	0.55117(3)	0.0134(2)
Ga1	0.0938(2)	1/4	0.43178(8)	0.0183(5)
Ga2	0.3600(2)	1/4	0.29650(8)	0.0193(5)
Se1	0.02883(19)	1/4	0.56221(10)	0.0308(6)
Se2	0.04544(18)	1/4	0.24153(7)	0.0175(4)
Se3	0.15274(19)	1/4	0.35578(7)	0.0221(5)
Se4	0.2293(2)	1/4	0.76663(7)	0.0226(5)
Se5	0.26155(18)	1/4	0.47666(7)	0.0171(4)
Se6	0.32097(17)	1/4	0.15734(7)	0.0158(4)
Se7	0.45826(18)	1/4	0.36766(6)	0.0156(4)
O1	0.0532(10)	1/4	0.0273(4)	0.010(2)
O2	0.3425(12)	1/4	0.5893(4)	0.016(3)
$Nd_4Ga_2Se_7O_2$				
Nd1	0.23483(7)	1/4	0.05879(3)	0.01310(17)
Nd2	0.36539(7)	1/4	0.66795(3)	0.01344(17)
Nd3	0.50007(8)	1/4	0.81498(3)	0.0213(2)
Nd4	0.53512(7)	1/4	0.55101(3)	0.01246(17)
Ga1	0.09313(15)	1/4	0.43170(6)	0.0175(3)
Ga2	0.35536(15)	1/4	0.29763(6)	0.0182(4)
Se1	0.03008(15)	1/4	0.56236(8)	0.0345(5)
Se2	0.04269(13)	1/4	0.24066(5)	0.0165(3)
Se3	0.14957(14)	1/4	0.35491(5)	0.0207(3)
Se4	0.23044(15)	1/4	0.76575(6)	0.0216(3)
Se5	0.26164(13)	1/4	0.47636(5)	0.0155(3)
Se6	0.31871(13)	1/4	0.15716(5)	0.0142(3)
Se7	0.45704(13)	1/4	0.36813(5)	0.0144(3)
O1	0.0539(8)	1/4	0.0280(3)	0.0115(19)
O2	0.3445(9)	1/4	0.5886(3)	0.015(2)

[a]All atoms are located in Wyckoff position 4*c*. [b]U_{eq} is defined as one-third of the trace of the orthogonalized U_{ij} tensor.

2.5. Electrochemical Measurements. Materials were carbon cloth (MSE Supplies), Nafion (5 wt %, Sigma-Aldrich), isopropanol (Sigma), and potassium hydroxide (Fisher). Millipore system purified and deionized water was used in all experiments. The carbon cloth was rinsed with isopropanol and water multiple times to ensure a clean surface before use. The cleaned carbon cloth substrates were dried and covered with Teflon tape, exposing only a circular area of 0.283 cm^2. Catalyst inks were prepared by dispersing 10.0 mg of the catalyst in 1.0 mL of 0.8% Nafion in isopropanol and ultrasonicating for 30 min. A 20 μL volume of ink was pipetted out for each catalyst and drop-cast on the exposed area of the carbon cloth substrate. After being dried at room temperature and then at 60 °C for 3 h, these substrates were used as the working electrodes.

Electrochemical measurements were performed using a conventional three-electrode system connected to an IviumStat potentiostat with catalyst-loaded carbon cloth as the working electrode, graphite rod as the counter electrode, and Ag|AgCl as the reference electrode. Linear sweep voltammetry (LSV) and cyclic voltammetry (CV) were carried out to examine the OER catalytic performance and cycling

https://doi.org/10.1021/acs.chemmater.3c02842
Chem. Mater. 2024, 36, 937−948

Table 3. Interatomic Distances (Å) in $RE_4Ga_2Se_7O_2$ (RE = Pr, Nd)

	$Pr_4Ga_2Se_7O_2$	$Nd_4Ga_2Se_7O_2$
*RE*1−Se6	3.079(2)	3.070(2)
*RE*1−Se5 (×2)	3.153(2)	3.143(1)
*RE*1−Se1 (×2)	3.404(2)	3.389(2)
*RE*1−O1	2.341(11)	2.301(9)
*RE*1−O2 (×2)	2.372(7)	2.361(6)
*RE*2−Se6 (×2)	2.959(2)	2.943(1)
*RE*2−Se7 (×2)	3.080(2)	3.062(1)
*RE*2−Se2 (×2)	3.133(2)	3.117(1)
*RE*2−Se4	3.309(2)	3.295(2)
*RE*2−O2	2.358(12)	2.359(10)
*RE*3−Se3 (×2)	2.900(2)	2.896(1)
*RE*3−Se6 (×2)	3.024(2)	3.016(1)
*RE*3−Se2 (×2)	3.025(2)	3.003(1)
*RE*3−Se4	3.465(3)	3.470(2)
*RE*4−Se7 (×2)	3.126(2)	3.109(1)
*RE*4−Se5 (×2)	3.211(2)	3.198(1)
*RE*4−O1	2.334(12)	2.348(10)
*RE*4−O1 (×2)	2.358(6)	2.341(5)
*RE*4−O2	2.529(14)	2.489(11)
Ga1−Se3	2.357(3)	2.365(2)
Ga1−Se5	2.374(3)	2.371(2)
Ga1−Se1 (×2)	2.464(2)	2.457(2)
Ga2−Se7	2.403(3)	2.400(2)
Ga2−Se4 (×2)	2.420(2)	2.414(1)
Ga2−Se2	2.449(3)	2.464(2)
Ga2−Se3	2.998(3)	2.941(2)

stability. To reduce uncompensated solution resistance, all activity data were *iR*-corrected, as measured through electrochemical impedance studies. The electrolytes for OER were saturated by bubbling with oxygen before and during the experiments. The measured potentials (in units of V) were calibrated to a reversible hydrogen electrode (RHE) using the following equation:

$$E_{RHE} = E_{Ag/AgCl} + 0.197 + 0.059pH \quad (1)$$

Electrochemical impedance spectroscopy (EIS) experiments were performed within a frequency range of 10^5−10^{-2} Hz at an AC signal amplitude of 10 mV to study the electrode kinetics and to estimate the electrolyte resistance (R_1) and charge transfer resistance (R_2) at the interface between the electrode (catalyst) and electrolyte. Nyquist plots were collected in N_2-saturated 1.0 M KOH solution at an applied potential of 0.55 V vs Ag|AgCl (KCl saturated).

The steady-state performance and durability of $Pr_4Ga_2Se_7O_2$ as an electrocatalyst for the OER were evaluated by chronoamperometric stability experiments in N_2-saturated 1.0 M KOH solution at room temperature. Two conditions were applied: (i) at a constant current density of 10 mA cm^{-2} for 24 h and (ii) at various current densities between 5 and 30 mA cm^{-2} in a multistep study.

Additional details of the electrochemical experiments, including analysis of Tafel plots, turnover frequency (TOF), mass activity, electrochemically active surface area (ECSA), and roughness factor (RF), are provided in the Supporting Information.

2.6. X-ray Photoelectron Spectroscopy (XPS). XPS experiments were carried out on a Kratos AXIS 165 photoelectron spectrometer equipped with a monochromatic Al Kα X-ray source (1487 eV) operating under a high vacuum in the analytical chamber. Pristine surfaces of $RE_4Ga_2Se_7O_2$ (RE = Pr, Nd) were examined without sputtering. The spectra were calibrated by setting the C 1s binding energy (BE) of adventitious carbon to 284.8 eV and analyzed using the CasaXPS software program.[59] The survey spectra confirmed the presence of all of the expected elements. The high-resolution spectra were analyzed by removing the background with a Shirley function and fitting with Lorentzian asymmetric lineshapes. Additional constraints were applied to individual positions, line widths (as evaluated by the full width at half-maximum, fwhm), and areas of peaks during the curve fitting procedure.

3. RESULTS AND DISCUSSION

3.1. Structure. The oxyselenides $Pr_4Ga_2Se_7O_2$ and $Nd_4Ga_2Se_7O_2$, which are the first quaternary phases known in these systems, were prepared as pure-phase samples. Because crystals of these compounds were thin and fibrous, considerable effort was expended to screen suitable samples for single-crystal X-ray diffraction analysis. The orthorhombic structure (space group *Pnma*) is a new type, consisting of four *RE*, two Ga, seven Se, and two O sites, all lying on mirror planes. For the purpose of describing the structure, it is helpful to identify three types of building blocks that extend along the *b*-direction: *RE*−O, *RE*−Se, and Ga−Se (Figure 2). The *RE*−

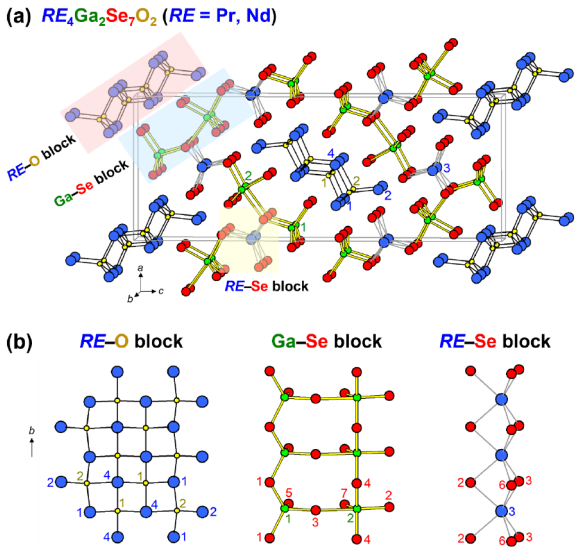

Figure 2. (a) Structure of $RE_4Ga_2Se_7O_2$ (RE = Pr, Nd) in terms of (b) *RE*−O, Ga−Se, and *RE*−O blocks that extend along the *b*-direction. The colored numbers label sites for *RE* (blue), Ga (green), Se (red), and O (yellow) atoms.

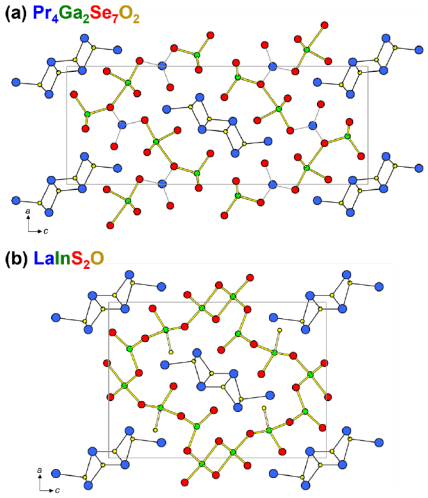

Figure 3. Comparison of (a) $Pr_4Ga_2Se_7O_2$ and (b) orthorhombic $LaInS_2O$, showing similar arrangements of edge-sharing RE_4O tetrahedra.

https://doi.org/10.1021/acs.chemmater.3c02842
Chem. Mater. 2024, 36, 937−948

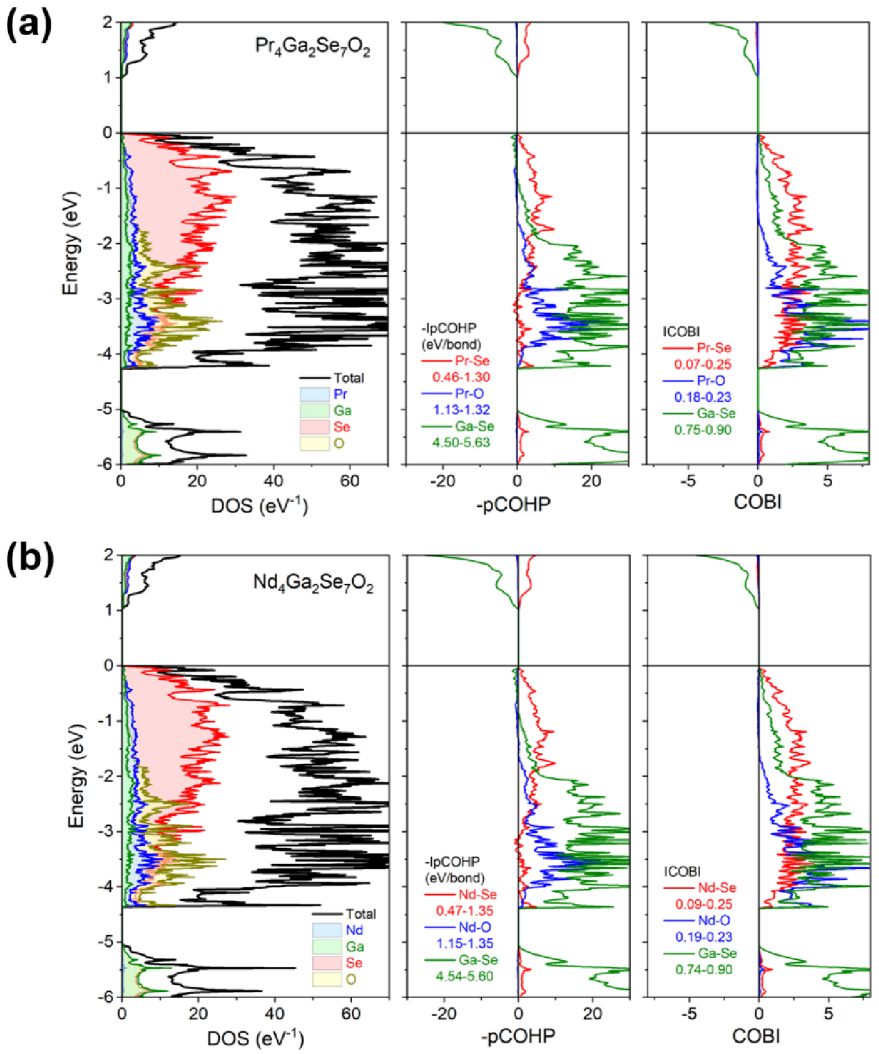

Figure 4. DOS (left), −pCOHP (center), and COBI (right) curves for (a) $Pr_4Ga_2Se_7O_2$ and (b) $Nd_4Ga_2Se_7O_2$.

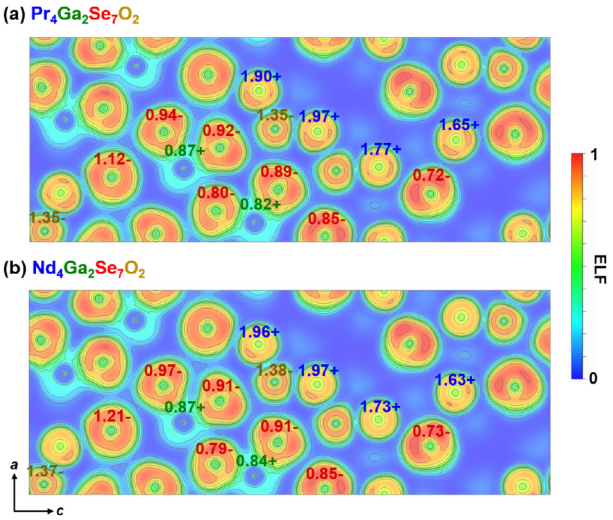

Figure 5. ELF plots viewed on a slice at $y = 1/4$ for (a) $Pr_4Ga_2Se_7O_2$ and (b) $Nd_4Ga_2Se_7O_2$. Bader charges are indicated for atoms identified by the color scheme shown in the chemical formulas.

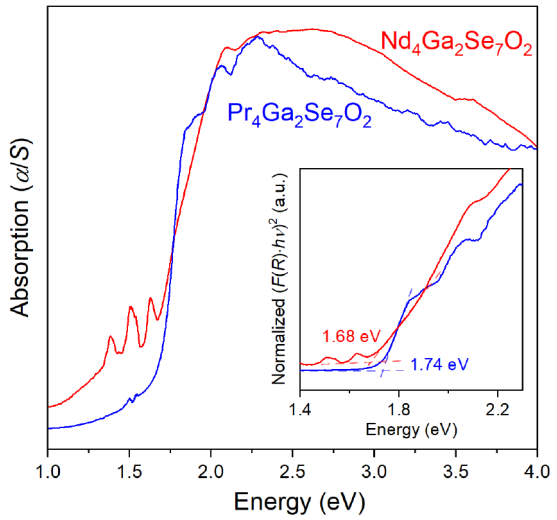

Figure 6. Optical diffuse reflectance spectra, converted to absorption spectra, for $Pr_4Ga_2Se_7O_2$ and $Nd_4Ga_2Se_7O_2$. The inset shows Tauc plots, assuming direct band gaps.

O blocks are strips of edge-sharing RE_4O tetrahedra that are four units thick. The RE−Se blocks are one-dimensional confacial columns of $RESe_6$ trigonal prisms (CN6). The Ga−Se blocks are the most interesting, consisting of chains of

https://doi.org/10.1021/acs.chemmater.3c02842
Chem. Mater. 2024, 36, 937−948

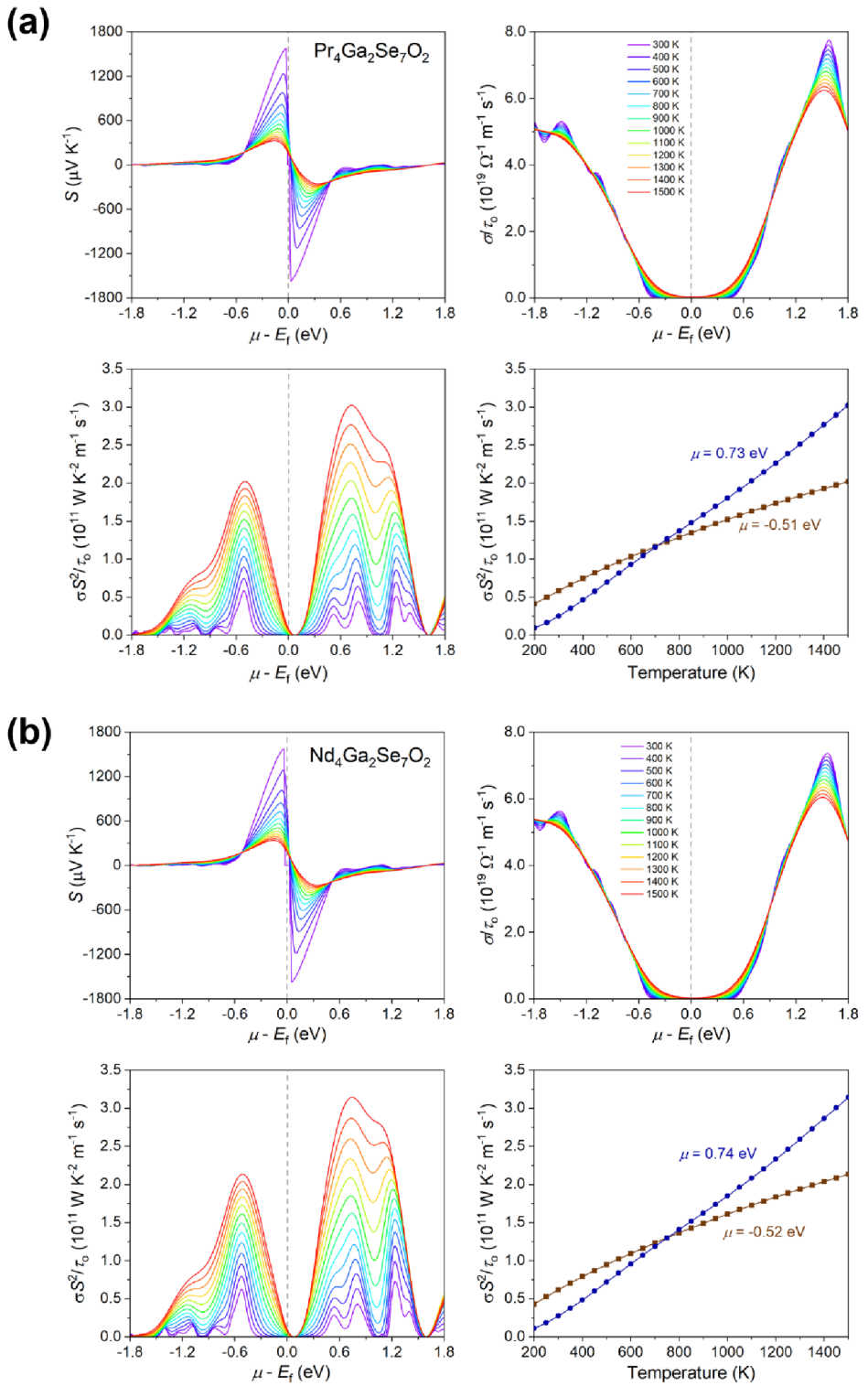

Figure 7. Calculated thermal transport properties for (a) $Pr_4Ga_2Se_7O_2$ and (b) $Nd_4Ga_2Se_7O_2$: Dependence of Seebeck coefficient (upper left panel), electrical conductivity (upper right panel), and power factor with chemical potential (lower left panel); and dependence of power factor with temperature (lower right panel).

corner-sharing $GaSe_4$ tetrahedra and $GaSe_5$ trigonal bipyramids. These Ga−Se blocks are linked by *RE*−Se blocks, resulting in corrugated layers between which the *RE*−O blocks are inserted. However, bonding extends in all three dimensions in this framework structure, because the *RE* atoms within the *RE*−O blocks form bonds to nearby Se atoms within the other blocks. The *RE* atoms exhibit high coordination numbers: *RE*3 is surrounded by six Se atoms at distances of 2.9−3.0 Å in a trigonal prism, with an additional Se atom further away at 3.5 Å to give a monocapped trigonal prismatic geometry (CN7), whereas *RE*1, *RE*2, and *RE*4 are surrounded by a combination of Se and O atoms in bicapped trigonal prismatic geometry (CN8) (Figure S2). These coordination geometries are similar to those found in Sm_3GaSe_5O.[38] The longer *RE*−Se distances

https://doi.org/10.1021/acs.chemmater.3c02842
Chem. Mater. 2024, 36, 937−948

Table 4. Electrocatalytic Performance of $RE_4Ga_2Se_7O_2$ (*RE* = Pr, Nd)

	$Pr_4Ga_2Se_7O_2$	$Nd_4Ga_2Se_7O_2$
onset potential (V)	1.47	1.52
overpotential at 10 mA cm^{-2} (mV)	257	328
preoxidation peaks (V)	1.45	1.49
Tafel slope (mV dec^{-1})	58.8	217.5
mass activity at η = 0.30 V (A g^{-1})	70.1	7.5
TOF at η = 0.30 V (s^{-1})	0.0234	0.00248
ECSA (cm^2)	106.3	92.4
RF	375.6	326.5

of 2.9−3.5 Å and the shorter *RE*−O distances of 2.3−2.5 Å agree with typical values found in binary *RE* selenides or oxides (e.g., 2.99−3.18 Å in Pr_2Se_3, 2.97−3.17 Å in Nd_2Se_3, 2.34 Å in PrO_2, and 2.29 Å in Nd_2O_3).[60−63]

The edge-sharing RE_4O tetrahedra, which are fragments of the fluorite-type structure, are a recurring theme in rare-earth oxychalcogenides.[44,45] They are usually manifested as two-dimensional slabs, as found in many layered oxychalcogenides (e.g., LaCuSO[20] and $RE_4Ga_2S_5O_4$[29,34,35]) but can be excised further into strips of varying widths,[64] as found here and other instances (e.g., Sm_3GaSe_5O[38] and $La_4Ga_2Se_6O_3$[40]). The strips of RE_4O tetrahedra in $RE_4Ga_2Se_7O_2$ are arranged in the same herringbone pattern as in an orthorhombic polymorph of $LaInS_2O$, which also crystallizes in space group *Pnma* with an identical Wyckoff sequence (c^{15}),[33] but the connectivity of the group-13 and chalcogen atoms is quite different (Figure 3).

The same motifs of corner-sharing $GaSe_4$ tetrahedra and $GaSe_5$ trigonal bipyramids in $RE_4Ga_2Se_7O_2$ are present in Sm_3GaSe_5O, recently discovered.[38] Five-coordinate $GaCh_5$ units are rare: GaO_5 has been reported in a few compounds,[65,66] GaS_5 is unknown, and $GaSe_5$ found here represents only the second occurrence. The coordination environment is quite regular around the tetrahedral Ga1 center, as reflected by the more uniform Ga−Se distances (2.36−2.46 Å) and angles (103.9−116.3°) in $Pr_4Ga_2Se_7O_2$. The trigonal bipyramidal Ga2 center shows a Ga−Se distance (3.00 Å) that is significantly longer than the other four (2.40−2.45 Å), so one may wonder if the coordination is more properly described as CN4 + 1. It is clear that the angles around Ga2 (111.0−121.9° for equatorial-equatorial and 82.2−102.4° for axial−equatorial ligands) are more consistent with a trigonal bipyramid than a tetrahedron. An analysis of the longer Ga−Se distance is presented below. For comparison, the $GaSe_5$ trigonal bipyramid in Sm_3GaSe_5O has four Ga−Se distances of 2.37−2.57 Å and a fifth longer distance of 2.79 Å.[38]

3.2. Bonding. The structure conforms to a charge-balanced formulation, $(RE^{3+})_4(Ga^{3+})_2(Se^{2-})_7(O^{2-})_2$, in generally good agreement with bond valence sums (Table S1).[67] The bond

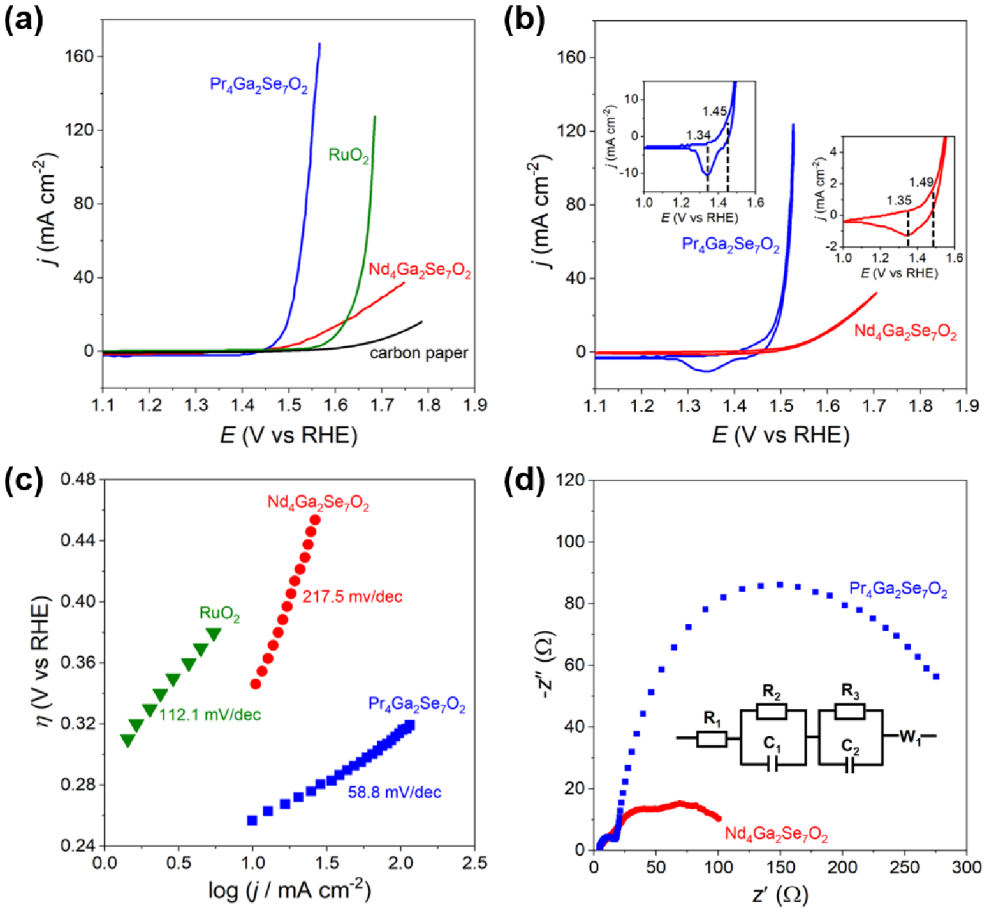

Figure 8. Electrocatalytic performance of $Pr_4Ga_2Se_7O_2$ and $Nd_4Ga_2Se_7O_2$. (a) Linear scan voltammetry (compared to RuO_2) at a scan rate of 10 mV s^{-1}. (b) Cyclic voltammetry at a scan rate of 10 mV s^{-1}, with insets showing detail. (c) Tafel plots. (d) Nyquist plots from electrochemical impedance spectroscopy performed with an AC frequency range of 100 kHz to 0.1 Hz (at 1.45 V vs RHE) and fitted to the equivalent circuit shown.

https://doi.org/10.1021/acs.chemmater.3c02842
Chem. Mater. 2024, 36, 937−948

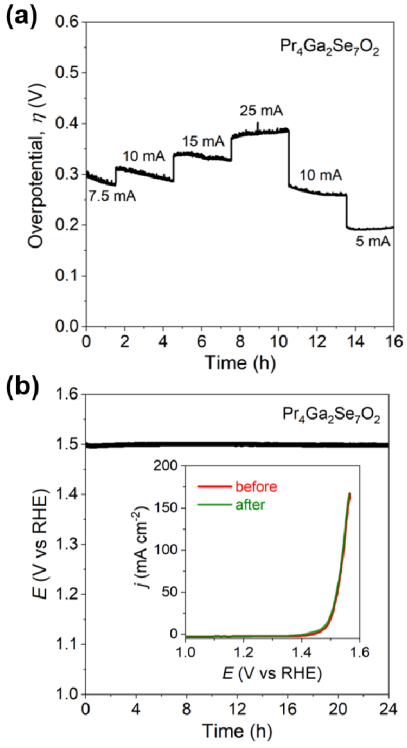

Figure 9. Chronoamperometry of $Pr_4Ga_2Se_7O_2$ at (a) various current densities with multisteps and (b) constant current density.

valence sum around the tetrahedral Ga1 atoms comes out as 3.0, in agreement with their expected valence. However, the trigonal bipyramidal Ga2 atom is slightly underbonded, with a bond valence sum of 2.8, if the distant fifth Se atom is neglected; including it restores the bond valence sum to 3.0. In general, the bond valence sums for all of the atoms exhibit a typical pattern in which some atoms are slightly underbonded and some are overbonded, implying that the structure results from a compromise between compressed and stretched bonds. The discrepancies between the expected bond valence sums and the atomic valences can be averaged over the entire structure to give a global instability index, which gives a measure of how much the structure is strained.[68] For both $Pr_4Ga_2Se_7O_2$ and $Nd_4Ga_2Se_7O_2$, the global instability index is 0.04, less than a limiting value of 0.10, which indicates that the structure is stable and well determined.

Electronic structure calculations show indirect band gaps of 0.98 eV for $Pr_4Ga_2Se_7O_2$ and 1.10 eV for $Nd_4Ga_2Se_7O_2$, but because the topmost valence bands are quite flat, these gaps are nearly direct (Figure S3). The DOS, −pCOHP, and COBI curves are plotted (Figure 4). The valence band is dominated by filled Ga 4p, Se 4p, and O 2p states, and the conduction band is dominated by empty *RE* 5d states. As is typical of valence-precise compounds, the band gap arises from optimization of bonding interactions: all bonding Ga−Se states are filled, and all antibonding Ga−Se states are empty. In contrast, the *RE*−Se and *RE*−O interactions do not contribute significantly; instead, they are expected to have more ionic character. Accordingly, the integrated −pCOHP values are largest for the more covalent Ga−Se interactions and relatively low for the more ionic *RE*−Se and *RE*−O interactions. The degree of bonding character can be further quantified from the COBI values, which range from 1 (strongly covalent) to 0 (strongly ionic). In agreement with expectations, the integrated COBI values are high for Ga−Se interactions (0.7−0.9) but low for *RE*−Se and *RE*−O interactions (0.1−0.2). Closer inspection of the −pCOHP curves for individual Ga−Se interactions shows that the long distance to the axial Se atom within the Ga-centered trigonal bipyramids corresponds to real bonding, arising from the surplus of filled bonding over antibonding levels (Figure S4). Its integrated −pCOHP value is about 25−30% that of the shorter Ga−Se distances.

The delineation of the structure in terms of more covalent Ga−Se blocks vs more ionic *RE*−Se and *RE*−O blocks can be visualized in ELF plots (Figure 5). Electron density is shared in the region between Ga and Se atoms, as indicated by the blue-green colors, but is much lower in the region between *RE* and Se atoms or between *RE* and O atoms, as indicated by the blue colors. Accordingly, the Bader charges are less extreme around Ga atoms (0.8+ to 0.9+) than around *RE* atoms (1.6+ to 2.0+), even though they are both formally 3+ cations. Similarly, they are less extreme around Se atoms (0.7− to 1.1−) than around O atoms (1.3− to 1.4−), even though they are both formally 2− anions.

3.3. Optical Properties. Optical diffuse reflectance spectra were collected on phase-pure powder samples (Figure 6). The sharp peaks found at lower energies to the absorption edge arise from f−f transitions of the *RE* atoms. Given that the band structure calculations indicated a nearly direct gap, Tauc plots were fitted with this assumption.[69] The measured optical band gaps are 1.74 eV for $Pr_4Ga_2Se_7O_2$ and 1.68 eV for $Nd_4Ga_2Se_7O_2$, consistent with the dark brown colors of both samples. If indirect band gaps are assumed, then they are 1.68 eV for $Pr_4Ga_2Se_7O_2$ and 1.66 eV for $Nd_4Ga_2Se_7O_2$ (Figure S5). The calculated band gaps presented earlier are underestimated by about 0.7 eV, as is typical when standard functionals are used. When the calculations were repeated using a hybrid HSE06 functional (with a PBE-to-Hartree−Fock ratio of 75:25), the predicted band gaps of 1.52 eV for $Pr_4Ga_2Se_7O_2$ and 1.58 eV for $Nd_4Ga_2Se_7O_2$ are in better agreement with the experimental values (Figure S6).

3.4. Calculated Thermoelectric Properties. Like other oxychalcogenides, $Pr_4Ga_2Se_7O_2$ and $Nd_4Ga_2Se_7O_2$ may be potential thermoelectric materials given their semiconducting behavior and high effective masses (as judged by the presence of flat bands near the Fermi level). Efforts were made to measure the experimental thermoelectric properties. About 3.5 g each of $Pr_4Ga_2Se_7O_2$ and $Nd_4Ga_2Se_7O_2$ were prepared. Many attempts were made to densify these samples by spark plasma sintering, but they resulted in pellets that cracked upon retrieval. Cracking may occur for various reasons, but overpressing and inappropriate thermal treatment rates were ruled out because many processing conditions were tried without success. It is possible that volume changes associated with phase transformations may be occurring at high temperatures, but this requires further investigation.

In the face of these difficulties, some of the thermoelectric properties were calculated to ascertain whether further experimental effort was worthwhile. As a reminder, for good thermoelectric materials, it is desirable to find high Seebeck coefficients S, high electrical conductivities σ, and low thermal conductivities κ. The thermoelectric figure of merit ZT is directly proportional to the power factor, $PF = \sigma S^2$, which is relatively straightforward to calculate and evaluate here. Thermal transport properties were calculated to examine how the Seebeck coefficients, electrical conductivities, and power factors depend on the chemical potential μ and

https://doi.org/10.1021/acs.chemmater.3c02842
Chem. Mater. 2024, 36, 937−948

temperature (varying from 300 to 1500 K) (Figure 7). These properties show little dependence on the *RE* substitution. For both compounds, the Seebeck coefficients reach maximum values of around ±1600 μV K^{-1} at 300 K within chemical potentials of ±0.05 eV from the Fermi level, and they decrease at higher temperatures, shifting away from μ = 0. At S = 0, the chemical potential range narrows to ±0.5 eV at all temperatures, which is attributed to easier electronic excitations. The temperature dependence of chemical potential and relaxation time, as well as the occurrence of greater scattering at high temperatures, should be taken into account to compare with experimental measurements.

The electrical conductivities were calculated within the constant relaxation time approximation. The electrical conductivities and power factors attain significantly higher maxima for n-doping (positive μ) than for p-doping (negative μ). If typical relaxation times of 10^{-15} to 10^{-14} s^{-1} are assumed, then the power factors are calculated to be 10^{-4} to 10^{-3} W K^{-2} m^{-1}, similar to those of other oxychalcogenides. The interpretation of these calculations is that $Pr_4Ga_2Se_7O_2$ and $Nd_4Ga_2Se_7O_2$ may be favorable candidates for n-doped thermoelectric materials, which remain relatively undeveloped compared to p-doped counterparts. Among n-doped oxychalcogenides, power factors have been experimentally found to be as high as 4.5 × 10^{-4} W K^{-2} m^{-1} for $LaBiS_{1.2}Se_{0.8}O$ at 743 K or 2.4 × 10^{-4} W K^{-2} m^{-1} for $Bi_2O_2Se_{0.985}Cl_{0.015}$.[11]

3.5. Electrocatalytic Properties. Electrocatalytic performance for the OER was evaluated in alkaline solution (1 M KOH) using a three-electrode system. Table 4 lists parameters extracted from the electrochemical analysis.

The OER polarization plots obtained from LSV show that $Pr_4Ga_2Se_7O_2$ exhibits higher catalytic activity than $Nd_4Ga_2Se_7O_2$ and the benchmark material RuO_2 (Figure 8a). At a current density of 10 mA cm^{-2}, the overpotential is lower for $Pr_4Ga_2Se_7O_2$ (257 mV) compared to $Nd_4Ga_2Se_7O_2$ (328 mV) and RuO_2 (370 mV). In the CV plots, preoxidation peaks before the onset of water oxidation appear as shoulders at 1.45 V for $Pr_4Ga_2Se_7O_2$ and 1.49 V for $Nd_4Ga_2Se_7O_2$ (Figure 8b); these peaks are typically attributed to catalyst site activation through attachment of an intermediate -OH group in OER. Tafel plots generated from the LSV curves reveal that $Pr_4Ga_2Se_7O_2$ has the smallest slope (58.8 mV dec^{-1}), implying fast OER kinetics (Figure 8c), consistent with its high mass activity (70.1 A g^{-1}) and TOF (0.0234 s^{-1}). As ascertained from CVs measured at different scan rates (Figure S7), $Pr_4Ga_2Se_7O_2$ has higher ECSA (106.3 cm^2) and RF (375.6), implying a greater number of electrochemically active sites and thereby facilitating electrolyte infiltration and interfacial interaction.

To probe the charge transfer kinetics at the electrode−electrolyte interface, EIS experiments were performed. The Nyquist plots for $Pr_4Ga_2Se_7O_2$ and $Nd_4Ga_2Se_7O_2$, each with two semicircular curves, indicate coupling of the electron transfer process with a surface adsorbed species (Figure 8d).[70] The EIS data were fit to an equivalent circuit consisting of electrolyte resistance R_1, charge transfer resistances R_2 and R_3, constant phase elements C_1 and C_2, and Warburg impedance W_1 attributed to charge diffusion from the electrolyte to the electrode or vice versa (Table S2). $Pr_4Ga_2Se_7O_2$ shows smaller charge-transfer resistance at the electrode−electrolyte interface, which corroborates well with the low Tafel slope and higher OER catalytic efficiency exhibited by this compound compared with the Nd analogue. The conductivity of the catalysts is slightly underestimated, because the interface contact is reduced when polymer binders are used to adhere the catalysts to the substrate. $Pr_4Ga_2Se_7O_2$ exhibits the minimum R_2 value of 8.65 Ω at a potential of 1.45 V (vs RHE), consistent with faster charge transfer kinetics.

Chronoamperometry was carried out to evaluate the stability performance of $Pr_4Ga_2Se_7O_2$ at different current density steps (Figure 9a) and to investigate the long-term durability at a constant potential of 1.46 V maintained for 24 h (Figure 9b). No significant deterioration was observed under uninterrupted OER, as seen in the polarization curves before and after the stability study (inset of Figure 9b). These results confirm that $Pr_4Ga_2Se_7O_2$ is robust and does not rapidly degrade during OER.

High-resolution XPS spectra collected before and after the electrocatalysis experiments were deconvoluted into component peaks (Figures S8 and S9; Table S3). The *RE* 3d spectra were fit to $3d_{5/2}$ and $3d_{3/2}$ components split by spin−orbit coupling at a separation of 20.3 eV in $Pr_4Ga_2Se_7O_2$ and 22.5 eV in $Nd_4Ga_2Se_7O_2$, with satellite features attributed to coupling with 4f electrons and shakeup processes.[71] In general, the BEs extracted from the *RE* 3d, Ga 3d and 2p, Se 3d, and O 1s spectra are consistent with the expected valence states (RE^{3+}, Ga^{3+}, Se^{2-}, and O^{2-}).[72] After the OER, the Ga 3d and O 1s spectra for $Pr_4Ga_2Se_7O_2$ show new peaks that were tentatively assigned based on the assumption that they arise from binding of surface-adsorbed hydroxide and H_2O/O_2 species. For $Nd_4Ga_2Se_7O_2$, the spectra were much less significantly affected, suggesting only mild surface oxidation. The superior electrocatalytic performance of the Pr member is an interesting result that appears to be observed in other *RE*-containing catalysts for water splitting, including perovskites and alloys.[73−76] However, given the XPS results, it is unlikely that it originates from involvement of a Pr^{4+}/Pr^{3+} couple, but perhaps through mechanisms like those in GaSe, which undergoes similar changes in its Ga 3d and Se 3d XPS spectra.[77,78]

4. CONCLUSIONS

The rare-earth oxyselenides $Pr_4Ga_2Se_7O_2$ and $Nd_4Ga_2Se_7O_2$ adopt a new structure type containing $GaSe_5$ trigonal bipyramids, only the second instance observed of such units. The segregation into more ionic *RE*−O and *RE*−Se blocks vs more covalent Ga−Se blocks reinforces this recurring theme found in many oxychalcogenides. These compounds are semiconductors with a nearly direct band gap of 1.7 eV, dictated by the crossover from bonding to antibonding Ga−Se interactions at the Fermi level. Calculations of thermal transport properties indicate higher power factors for positive chemical potentials, implying that n-doping could be applied to enhance their potential as thermoelectric materials. $Pr_4Ga_2Se_7O_2$ shows promising characteristics as an electrocatalyst for the OER, but more remains to be done to understand its mechanism.

■ ASSOCIATED CONTENT

Supporting Information

The Supporting Information is available free of charge at https://pubs.acs.org/doi/10.1021/acs.chemmater.3c02842.

Electrochemical analysis, bond valence sums, equivalent circuit parameters, XPS binding energies, SEM images, EDX spectra, coordination polyhedra, electronic struc-

https://doi.org/10.1021/acs.chemmater.3c02842
Chem. Mater. 2024, 36, 937−948

ture calculations, cyclic voltammograms, and high-resolution XPS spectra (PDF)

Accession Codes

CCDC 2266497−2266498 contain the supplementary crystallographic data for this paper. These data can be obtained free of charge via www.ccdc.cam.ac.uk/data_request/cif, or by emailing data_request@ccdc.cam.ac.uk, or by contacting The Cambridge Crystallographic Data Centre, 12 Union Road, Cambridge CB2 1EZ, UK; fax: + 44 1223 336033.

AUTHOR INFORMATION

Corresponding Authors

Manashi Nath − *Department of Chemistry, Missouri University of Science and Technology, Rolla, Missouri 65409, United States;* orcid.org/0000-0002-5058-5313; Email: nathm@mst.edu

Arthur Mar − *Department of Chemistry, University of Alberta, Edmonton, Alberta T6G 2G2, Canada;* orcid.org/0000-0003-0474-5918; Email: amar@ualberta.ca

Authors

Vidyanshu Mishra − *Department of Chemistry, University of Alberta, Edmonton, Alberta T6G 2G2, Canada;* orcid.org/0000-0002-8660-2859

Ibrahim Munkaila Abdullahi − *Department of Chemistry, Missouri University of Science and Technology, Rolla, Missouri 65409, United States*

Dundappa Mumbaraddi − *Department of Chemistry, University of Alberta, Edmonton, Alberta T6G 2G2, Canada;* orcid.org/0000-0003-3099-9348

Mohammed Jomaa − *Department of Chemistry, University of Alberta, Edmonton, Alberta T6G 2G2, Canada;* orcid.org/0000-0002-9904-1755

Louis Guérin − *Department of Chemistry, University of Alberta, Edmonton, Alberta T6G 2G2, Canada*

Complete contact information is available at: https://pubs.acs.org/10.1021/acs.chemmater.3c02842

Author Contributions

The manuscript was written through contributions of all authors. All authors have given approval to the final version of the manuscript.

Notes

The authors declare no competing financial interest.

ACKNOWLEDGMENTS

This work was supported by the Natural Sciences and Engineering Research Council of Canada (NSERC, through Discovery Grant No. RGPIN-2018-04294), the Canada First Research Excellence Fund (CFREF, through the Future Energy Systems Research Institute at the University of Alberta, Project No. T12-P01), and resources available through Digital Research Alliance of Canada (alliancecan.ca). M.N. and I.A.M. would also like to acknowledge financial support from NSF (no. CAS-2155175). We are grateful to Hasan M. Sayeed, Andrew Falkowski, and Professor Taylor Sparks at the University of Utah for their experimental attempts to prepare densified pellets.

REFERENCES

(1) Kageyama, H.; Hayashi, K.; Maeda, K.; Attfield, J. P.; Hiroi, Z.; Rondinelli, J. M.; Poeppelmeier, K. R. Expanding frontiers in materials chemistry and physics with multiple anions. *Nat. Commun.* **2018**, *9*, 772.

(2) Harada, J. K.; Charles, N.; Poeppelmeier, K. R.; Rondinelli, J. M. Heteroanionic materials by design: Progress toward targeted properties. *Adv. Mater.* **2019**, *31*, 1805295.

(3) Tripathi, T. S.; Karppinen, M. Mixed-anion compounds: An unexplored playground for ALD fabrication. *Adv. Mater. Interfaces* **2021**, *8*, 2100146.

(4) Villars, P.; Cenzual, K. *Pearson's Crystal Data − Crystal Structure Database for Inorganic Compounds (on DVD)*; Release 2021/22; ASM International: Materials Park, OH, USA.

(5) Ueda, K.; Hiramatsu, H.; Hirano, M.; Kamiya, T.; Hosono, H. Wide-gap layered oxychalcogenide semiconductors: Materials, electronic structures and optoelectronic properties. *Thin Solid Films* **2006**, *496*, 8−15.

(6) Clarke, S. J.; Adamson, P.; Herkelrath, S. J. C.; Rutt, O. J.; Parker, D. R.; Pitcher, M. J.; Smura, C. F. Structures, physical properties, and chemistry of layered oxychalcogenides and oxypnictides. *Inorg. Chem.* **2008**, *47*, 8473−8486.

(7) Hiramatsu, H.; Kamihara, Y.; Yanagi, H.; Ueda, K.; Kamiya, T.; Hirano, M.; Hosono, H. Layered mixed-anion compounds: Epitaxial growth, active function exploration, and device application. *J. Eur. Ceram. Soc.* **2009**, *29*, 245−253.

(8) Luu, S. D. N.; Vaqueiro, P. Layered oxychalcogenides: Structural chemistry and thermoelectric properties. *J. Materiomics* **2016**, *2*, 131−140.

(9) He, J.; Yao, Z.; Hegde, V. I.; Naghavi, S. S.; Shen, J.; Bushick, K. M.; Wolverton, C. Computational discovery of stable heteroanionic oxychalcogenides ABXO (A, B = metals; X = S, Se, and Te) and their potential applications. *Chem. Mater.* **2020**, *32*, 8229−8242.

(10) Shi, Y.-F.; Wei, W.-B.; Wu, X.-T.; Lin, H.; Zhu, Q.-L. Recent progress in oxychalcogenides as IR nonlinear optical materials. *Dalton Trans.* **2021**, *50*, 4112−4118.

(11) Tippireddy, S.; Prem Kumar, D. S.; Das, S.; Malik, R. C. Oxychalcogenides as thermoelectric materials: An overview. *ACS Appl. Energy Mater.* **2021**, *4*, 2022−2040.

(12) Yang, Y.; Han, J.; Zhou, Z.; Zou, M.; Xu, Y.; Zheng, Y.; Nan, C.-W.; Lin, Y.-H. Seeking new layered oxyselenides with promising thermoelectric performance. *Adv. Funct. Mater.* **2022**, *32*, 2113164.

(13) Yang, Y.; Zhou, Z.; Wei, B.; Liu, J.; Lan, J.-L.; Zou, M.; Xu, Y.; Zheng, Y.; Nan, C.-W.; Lin, Y.-H. Thermoelectric properties of layered oxyselenides with 3d transition metal ions. *J. Am. Ceram. Soc.* **2023**, *106*, 2918−2929.

(14) Li, B.-Q.; Zhang, S.-Y.; Tang, C.; Cui, X.; Zhang, Q. Anionic regulated NiFe (oxy)sulfide electrocatalysts for water oxidation. *Small* **2017**, *13*, 1700610.

(15) Zou, X.; Wu, Y.; Liu, Y.; Liu, D.; Li, W.; Gu, L.; Liu, H.; Wang, P.; Sun, L.; Zhang, Y. *In situ* generation of bifunctional, efficient Fe-based catalysts from mackinawite iron sulfide for water splitting. *Chem* **2018**, *4*, 1139−1152.

(16) Rajeshkhanna, G.; Kandula, S.; Shrestha, K. R.; Kim, N. H.; Lee, J. H. A new class of $Zn_{1-x}Fe_x$−oxyselenide and $Zn_{1-x}Fe_x$−LDH nanostructured material with remarkable bifunctional oxygen and hydrogen evolution electrocatalytic activities for overall water splitting. *Small* **2018**, *14*, 1803638.

(17) Balamurugan, J.; Nguyen, T. T.; Kim, D. H.; Kim, N. H.; Lee, J. H. 3D nickel molybdenum oxyselenide ($Ni_{1-x}Mo_xOSe$) nanoarchitectures as advanced multifunctional catalyst for Zn-air batteries and water splitting. *Appl. Catal., B* **2021**, *286*, 119909.

(18) Larquet, C.; Carenco, S. Metal oxysulfides: From bulk compounds to nanomaterials. *Front. Chem.* **2020**, *8*, 179.

(19) Mizuguchi, Y.; Omachi, A.; Goto, Y.; Kamihara, Y.; Matoba, M.; Hiroi, T.; Kajitani, J.; Miura, O. Enhancement of thermoelectric properties by Se substitution in layered bismuth-chalcogenide $LaOBiS_{2-x}Se_x$. *J. Appl. Phys.* **2014**, *116*, 163915.

(20) Ueda, K.; Inoue, S.; Hirose, S.; Kawazoe, H.; Hosono, H. Transparent *p*-type semiconductor: LaCuOS layered oxysulfide. *Appl. Phys. Lett.* **2000**, *77*, 2701−2703.

(21) Chen, Y.; Cui, Y.; Pham, A.; Wang, Y.; Bhadbhade, M. M.; Wang, R.; Su, Y.; Hu, H.; Wen, Z.; Cheng, C.; Tan, T. T.; Li, S.; Zhao, Y. Superconductivity and structural instability in layered BiS_2-based $LaO_{1-x}BiS_2$. *J. Mater. Chem. C* **2019**, *7*, 586−591.
(22) Wilmer, D.; Jorgensen, J. D.; Wuensch, B. J. Two-dimensional silver fast-ion conduction in (LaO)AgS. *Solid State Ionics* **2000**, *136*−*137*, 961−966.
(23) Ishikawa, A.; Takata, T.; Kondo, J. N.; Hara, M.; Kobayashi, H.; Domen, K. Oxysulfide $Sm_2Ti_2S_2O_5$ as a stable photocatalyst for water oxidation and reduction under visible light irradiation ($\lambda \leq 650$ nm). *J. Am. Chem. Soc.* **2002**, *124*, 13547−13553.
(24) Suen, N.-T.; Hung, S.-F.; Quan, Q.; Zhang, N.; Xu, Y.-J.; Chen, H. M. Electrocatalysis for the oxygen evolution reaction: Recent development and future perspectives. *Chem. Soc. Rev.* **2017**, *46*, 337−365.
(25) Wang, X.; Tang, Y.; Lee, J.-M.; Fu, G. Recent advances in rare-earth-based materials for electrocatalysis. *Chem. Catal.* **2022**, *2*, 967−1008.
(26) Guittard, M.; Pardo, M.-P.; Lourieau-Lozac'h, A.-M. Sur le système La_2O_2S−Ga_2S_3. *C. R. Seances Acad. Sci., Ser. C* **1977**, *284*, 37−39.
(27) Jaulmes, S. Oxysulfure de gallium et de lanthane $LaGaOS_2$. *Acta Crystallogr. Sect. B* **1978**, *34*, 2610−2612.
(28) Bénazeth, S.; Guittard, M.; Laruelle, P. Structure de l'oxyséléniure de lanthane et de gallium, $(LaO)GaSe_2$. *Acta Crystallogr. Sect. C* **1984**, *40*, 345−347.
(29) Guittard, M.; Bénazeth, S.; Dugué, J.; Jaulmes, S.; Palazzi, M.; Laruelle, P.; Flahaut, J. Oxysulfides and oxyselenides in sheets, formed by a rare earth element and a second metal. *J. Solid State Chem.* **1984**, *51*, 227−238.
(30) Kabbour, H.; Cario, L.; Moëlo, Y.; Meerschaut, A. Synthesis, X-ray and optical characterizations of two new oxysulfides: $LaInS_2O$ and $La_5In_3S_9O_3$. *J. Solid State Chem.* **2004**, *177*, 1053−1059.
(31) Miura, A.; Oshima, T.; Maeda, K.; Mizuguchi, Y.; Moriyoshi, C.; Kuroiwa, Y.; Meng, Y.; Wen, X.-D.; Nagao, M.; Higuchi, M.; Tadanaga, K. Synthesis, structure and photocatalytic activity of layered $LaOInS_2$. *J. Mater. Chem. A* **2017**, *5*, 14270−14277.
(32) Ito, H.; Miura, A.; Goto, Y.; Mizuguchi, Y.; Moriyoshi, C.; Kuroiwa, Y.; Azuma, M.; Liu, J.; Wen, X.-D.; Nishioka, S.; Maeda, K.; Masubuchi, Y.; Rosero-Navarro, N. C.; Tadanaga, K. An electronic structure governed by the displacement of the indium site in In−S_6 octahedra: $LnOInS_2$ (Ln = La, Ce, and Pr). *Dalton Trans.* **2019**, *48*, 12272−12278.
(33) Kabbour, H.; Sayede, A.; Saitzek, S.; Lefèvre, G.; Cario, L.; Trentesaux, M.; Roussel, P. Structure of the water-splitting photocatalyst oxysulfide α-$LaOInS_2$ and *ab initio* prediction of new polymorphs. *Chem. Commun.* **2020**, *56*, 1645−1648.
(34) Dugué, J.; Guittard, M. Structure de l'oxysulfure de néodyme et de gallium $(NdO)_4Ga_2S_5$. *Acta Crystallogr. Sect. B* **1982**, *38*, 2368−2371.
(35) Bénazeth, S.; Laruelle, P.; Guittard, M. Structure moyenne d'un oxyséléniure de lanthane et gallium $(LaO)_4Ga_{1.88}Se_{4.82}$. *J. Solid State Chem.* **1989**, *78*, 147−153.
(36) Mazurier, A.; Guittard, M.; Jaulmes, S. Structure cristalline d'un oxysulfure isotype de la mélilite, $La_{3.33}Ga_6O_2S_{12}$. *Acta Crystallogr. Sect. B* **1982**, *38*, 379−382.
(37) Jaulmes, S.; Mazurier, A.; Guittard, M. Structure de l'oxypentasulfure de gallium et de trilanthane, $GaLa_3OS_5$. *Acta Crystallogr. Sect. C* **1983**, *39*, 1594−1597.
(38) Mishra, V.; Mumbaraddi, D.; Iyer, A. K.; Yin, W.; Mar, A. Semiconducting Sm_3GaSe_5O with trigonal bipyramidal $GaSe_5$ units. *J. Solid State Chem.* **2022**, *308*, 122901.
(39) Gastaldi, L.; Carré, D.; Pardo, M. P. Structure de l'oxysulfure d'indium et de lanthane $In_6La_{10}O_6S_{17}$. *Acta Crystallogr. Sect. B* **1982**, *38*, 2365−2367.
(40) Mishra, V.; Zabolotnii, A.; Mar, A. $La_4Ga_2Se_6O_3$: A rare-earth oxyselenide built from one-dimensional strips. *Inorg. Chem.* **2022**, *61*, 12458−12465.
(41) Yan, H.; Fujii, K.; Kabbour, H.; Chikamatsu, A.; Meng, Y.; Matsushita, Y.; Yashima, M.; Yamaura, K.; Tsujimoto, Y. $La_4Ga_2S_8O_3$: A rare-earth gallium oxysulfide with disulfide ions. *Inorg. Chem.* **2023**, *62*, 10481−10489.
(42) Ogisu, K.; Ishikawa, A.; Teramura, K.; Toda, K.; Hara, M.; Domen, K. Lanthanum-indium oxysulfide as a visible light driven photocatalyst for water splitting. *Chem. Lett.* **2007**, *36*, 854−855.
(43) Ogisu, K.; Ishikawa, A.; Shimodaira, Y.; Takata, T.; Kobayashi, H.; Domen, K. Electronic band structures and photochemical properties of La−Ga-based oxysulfides. *J. Phys. Chem. C* **2008**, *112*, 11978−11984.
(44) Figueiredo, M. O. Crystal chemistry and layered structural description of oxychalcogenides involving f-transition elements. *Inorg. Chim. Acta* **1987**, *140*, 161−164.
(45) Orr, M.; Hebberd, G. R.; McCabe, E. E.; Macaluso, R. T. Structural diversity of rare-earth oxychalcogenides. *ACS Omega* **2022**, *7*, 8209−8218.
(46) Gazulla, M. F.; Ventura, M. J.; Andreu, C.; Gilabert, J.; Orduña, M.; Rodrigo, M. Praseodymium oxides. Complete characterization by determining oxygen content. *Microchem. J.* **2019**, *148*, 291−298.
(47) Sheldrick, G. M. A short history of *SHELX*. *Acta Crystallogr., Sect. A* **2008**, *64*, 112−122.
(48) Gelato, L. M.; Parthé, E. STRUCTURE TIDY − a computer program to standardize crystal structure data. *J. Appl. Crystallogr.* **1987**, *20*, 139−143.
(49) Hafner, J. *Ab-initio* simulations of materials using VASP: Density-functional theory and beyond. *J. Comput. Chem.* **2008**, *29*, 2044−2078.
(50) Perdew, J. P.; Burke, K.; Ernzerhof, M. Generalized gradient approximation made simple. *Phys. Rev. Lett.* **1996**, *77*, 3865−3868.
(51) Grin, Y.; Savin, A.; Silvi, B. The ELF perspective of chemical bonding. In: *The Chemical Bond: Fundamental Aspects of Chemical Bonding*; Frenking, G.; Shaik, S., Eds.; Wiley-VCH: Weinheim, 2014; pp 345−382.
(52) Momma, K.; Izumi, F. *VESTA 3* for three-dimensional visualization of crystal, volumetric and morphology data. *J. Appl. Crystallogr.* **2011**, *44*, 1272−1276.
(53) Tang, W.; Sanville, E.; Henkelman, G. A grid-based Bader analysis algorithm without lattice bias. *J. Phys.: Condens. Matter* **2009**, *21*, 084204.
(54) Deringer, V. L.; Tchougréeff, A. L.; Dronskowski, R. Crystal orbital Hamilton population (COHP) analysis as projected from plane-wave basis sets. *J. Phys. Chem. A* **2011**, *115*, 5461−5466.
(55) Müller, P. C.; Ertural, C.; Hempelmann, J.; Dronskowski, R. Crystal orbital bond index: Covalent bond orders in solids. *J. Phys. Chem. C* **2021**, *125*, 7959−7970.
(56) Maintz, S.; Deringer, V. L.; Tchougréeff, A. L.; Dronskowski, R. LOBSTER: A tool to extract chemical bonding from plane-wave based DFT. *J. Comput. Chem.* **2016**, *37*, 1030−1035.
(57) Madsen, G. K. H.; Carrete, J.; Verstraete, M. J. BoltzTraP2, a program for interpolating band structures and calculating semi-classical transport coefficients. *Comput. Phys. Commun.* **2018**, *231*, 140−145.
(58) Kortüm, G. *Reflectance Spectroscopy*; Springer: New York, 1969; pp 103−169.
(59) Fairley, N.; Fernandez, V.; Richard-Plouet, M.; Guillot-Deudon, C.; Walton, J.; Smith, E.; Flahaut, D.; Greiner, M.; Biesinger, M.; Tougaard, S.; Morgan, D.; Maltrusaitis, J. Systematic and collaborative approach to problem solving using X-ray photoelectron spectroscopy. *Appl. Surf. Sci. Adv.* **2021**, *5*, 100112.
(60) Folchnandt, M.; Schleid, T. Single crystals of C-La_2Se_3, C-Pr_2Se_3, and C-Gd_2Se_3 with cation-deficient Th_3P_4-type structure. *Z. Anorg. Allg. Chem.* **2001**, *627*, 1411−1413.
(61) Schneck, C.; Höss, P.; Schleid, T. C-type Nd_2Se_3. *Acta Crystallogr. Sect. E: Struct. Rep. Online* **2009**, *65*, i20.
(62) Kern, S.; Loong, C.-K.; Faber, J., Jr; Lander, G. H. Neutron scattering investigation of the magnetic ground state of PrO_2. *Solid State Commun.* **1984**, *49*, 295−298.

https://doi.org/10.1021/acs.chemmater.3c02842
Chem. Mater. 2024, 36, 937−948

(63) Artini, C.; Pani, M.; Plaisier, J. R.; Costa, G. A. Structural study of Nd oxidation by means of in-situ synchrotron X-ray diffraction ($400 \leq T \leq 700$ °C). *Solid State Ionics* **2014**, *257*, 38−41.
(64) Carré, D.; Guittard, M.; Jaulmes, S.; Mazurier, A.; Palazzi, M.; Pardo, M. P.; Laruelle, P.; Flahaut, J. Oxysulfides formed by a rare earth and a second metal: II. Shear structures. *J. Solid State Chem.* **1984**, *55*, 287−292.
(65) Shannon, R. D.; Prewitt, C. T. Synthesis and structure of phases in the In_2O_3−Ga_2O_3 system. *J. Inorg. Nucl. Chem.* **1968**, *30*, 1389−1398.
(66) Michiue, Y.; Kimizuka, N.; Kanke, Y. Structure of $Ga_2O_3(ZnO)_6$: A member of the homologous series $Ga_2O_3(ZnO)_m$. *Acta Crystallogr. Sect. B* **2008**, *64*, 521−526.
(67) Brese, N. E.; O'Keeffe, M. Bond valence parameters for solids. *Acta Crystallogr. Sect. B* **1991**, *47*, 192−197.
(68) Brown, I. D. Recent developments in the methods and applications of the bond valence model. *Chem. Rev.* **2009**, *109*, 6858−6919.
(69) Makuła, P.; Pacia, M.; Macyk, W. How to correctly determine the band gap energy of modified semiconductor photocatalysts based on UV-vis spectra. *J. Phys. Chem. Lett.* **2018**, *9*, 6814−6817.
(70) Harrington, D. A. The rate-determining step in electrochemical impedance spectroscopy. *J. Electroanal. Chem.* **2015**, *737*, 30−36.
(71) Crerar, S. J.; Mar, A.; Grosvenor, A. P. Electronic structure of rare-earth chromium antimonides *RE*$CrSb_3$ (*RE* = La−Nd, Sm, Gd−Dy, Yb) by X-ray photoelectron spectroscopy. *J. Solid State Chem.* **2012**, *196*, 79−86.
(72) NIST *NIST X-ray photoelectron spectroscopy database, NIST standard reference database number 20*; National Institute of Standards and Technology: Gaithersburg MD, 2000. DOI: DOI: 10.18434/T4T88K.
(73) Xu, X.; Chen, Y.; Zhou, W.; Zhu, Z.; Su, C.; Liu, M.; Shao, Z. A perovskite electrocatalyst for efficient hydrogen evolution reaction. *Adv. Mater.* **2016**, *28*, 6442−6448.
(74) Xie, R.; Nie, Z.; Hu, X.; Yu, Y.; Aruta, C.; Yang, N. Pr-doped $LaCoO_3$ toward stable and efficient oxygen evolution reaction. *ACS Appl. Energy Mater.* **2021**, *4*, 9057−9065.
(75) Zhu, W.; Chen, J.; Liu, D.; Yang, G.; Zhou, W.; Ran, R.; Yu, J.; Shao, Z. Engineering the oxygen-evolution activity by changing the A-site rare-earth elements in $RSr_3Fe_{1.5}Co_{1.5}O_{10-\delta}$ (R = La, Nd, Pr) Ruddlesden-Popper perovskites. *Mater. Chem. Front.* **2023**, *7*, 4526−4534.
(76) Zhang, S.; Sun, M.; Yin, L.; Wang, S.; Huang, B.; Du, Y.; Yan, C.-H. Tailoring the electronic structure of Ir alloy electrocatalysts through lanthanide (La, Ce, Pr, and Nd) for acidic oxygen evolution enhancement. *Adv. Energy Sustainability Res.* **2023**, *4*, 2300023.
(77) D'Olimpio, G.; Nappini, S.; Vorokhta, M.; Lozzi, L.; Genuzio, F.; Menteş, T. O.; Paolucci, V.; Gürbulak, B.; Duman, S.; Ottaviano, L.; Locatelli, A.; Bondino, F.; Boukhvalov, D. W.; Politano, A. Enhanced electrocatalytic activity in GaSe and InSe nanosheets: The role of surface oxides. *Adv. Funct. Mater.* **2020**, *30*, 2005466.
(78) Boukhvalov, D. W.; D'Olimpio, G.; Nappini, S.; Ottaviano, L.; Bondino, F.; Politano, A. III-IV and IV-VI van der Waals semiconductors InSe, GaSe, and GeSe: A suitable platform for efficient electrochemical water splitting, photocatalysis and chemical sensing. *Isr. J. Chem.* **2022**, *62*, No. e202100125.